DOI: 10.31276/VJSTE.2025.0048



# High-precision phase compensation in digital holographic microscopy via a Shack-Hartmann wavefront sensor in a telecentric configuration

**Pham Duc Tuan[1], Vu Thanh Tung[1*], Phan Dinh Tuan[1], Bui Thanh Tung[2], Mai Linh[2], Pham Ngoc Thao[2], Duong Minh Ngoc[2], Pham Duc Quang[2*]**

*[1]The School of Mechanical Engineering, Hanoi University of Science and Technology, Dai Co Viet Street, Bach Mai Ward, Hanoi, Vietnam*
*[2]University of Engineering and Technology (UET), Vietnam National University - Hanoi, 144 Xuan Thuy Street, Cau Giay Ward, Hanoi, Vietnam*

Received 17 June 2025; revised 23 June 2025; accepted 8 August 2025

***Abstract:***

**Digital holographic microscopy (DHM) enables the reconstruction of three-dimensional surface profiles with nanometre-scale axial resolution. However, measurement accuracy may be compromised by phase distortions arising from the spherical aberration of the microscope objective lens and by imperfections in other optical components. In this study, we propose a method that combines a Shack-Hartmann wavefront sensor (SH-WFS) with a reference - mirror arrangement, integrated within a telecentric optical system for phase compensation. This hybrid approach, which melds physical calibration with digital correction, simultaneously reduces both global and local system errors. Consequently, it achieves precise phase correction without complex manual adjustments and maintains high stability when switching between samples. Experiments were conducted using surface-roughness standards with arithmetic mean surface roughness values (Sa) of 20.3 and 11.6 nm, measured using a ZeGage™ Pro surface-scanning device. The results showed good agreement with the reference values provided by the ZeGage™ Pro, thereby confirming the effectiveness of the proposed method. Overall, this technique markedly improves measurement accuracy in DHM and underpins the development of highly automated measurement systems, offering promising applications in precision optics.**

***Keywords:*** **digital holographic microscope, phase aberration, phase error compensation, 3D surface measurement.**

***Classification numbers:*** **2.1, 2.3**

## 1. Introduction

Digital holographic microscopy (DHM) integrates holographic techniques with a conventional microscope system. Since its emergence in the early 21st century, DHM has attracted considerable interest from research groups worldwide. Unlike traditional microscopes, DHM employs digital holography to magnify specimen images while simultaneously capturing both phase and intensity information in a single hologram frame in the off-axis configuration used here. The phase data extracted from the hologram correspond directly to the surface depth of the object, as determined by the wavelength of the illuminating light. Consequently, DHM can achieve axial resolution on the order of several nanometres without requiring physical contact with the sample. Its simple system design, rapid measurement speed and high data throughput are key advantages [1-13]. These strengths have rendered DHM a powerful tool across diverse applications, including quality control of micro-electromechanical systems (MEMS) and micro-opto-electromechanical systems (MOEMS) [7-9], three-dimensional surface-contour measurements in precision machining [10, 11], and the detection and monitoring of changes in biological tissues [12, 13].

In both transmission and reflection configurations, the microscope objective (MO) plays a crucial role; however, it is also the principal source of phase distortion - particularly spherical aberration - which compromises measurement resolution and precision [5, 6, 14]. Misalignment between the hologram image plane and the receiver plane introduces further phase errors during object-surface reconstruction [15, 16]. Axial and transverse misalignment of optical components, together with their inherent quality, exacerbate these distortions [16, 17]. Phase aberrations may arise in both the reference and object arms of a DHM system [15, 16]. Proposed mitigation strategies generally fall into two categories: physical optical methods [4, 5, 18] and digital correction techniques [6, 14, 19]. Physical approaches principally target the spherical aberration introduced by the

*Corresponding author: Email: tung.vuthanh@hust.edu.vn; quangpd@vnu.edu.vn

MO by incorporating compensating optical elements such as electrically tunable lenses that generate a phase profile cancelling the distortion in the object arm or replicating it in the reference arm, thereby minimising phase error for highly reflective samples. Nevertheless, the integration of additional elements into the DHM system cannot fully correct high-order aberrations, leaving residual distortions. Conversely, digital methods-such as digital phase masks, simultaneous exposure techniques and synchronized acquisition-construct virtual phase maps to compensate for system aberrations. These methods depend on accurate system calibration and finely sampled data in conjunction with simulated phase-compensation algorithms, but they remain sensitive to noise and prone to error when the object is displaced from the reference plane, yielding reduced measurement precision. More recently, machine-learning techniques have emerged as a promising alternative for phase compensation [20-22]; however, they typically require large training datasets, posing practical challenges in DHM systems where rapid processing and high accuracy are essential.

Physical phase compensation utilising an infinity-corrected DHM configuration (4f system) has been shown to reduce spherical aberration caused by the MO effectively [14, 16, 18]. Yet previous studies have not introduced quantitative methods for measuring or correcting the residual phase components arising from the MO and other optical elements. In this work, an SH-WFS is employed to calibrate the system via direct wavefront measurement and analysis. A precision flat reference mirror is positioned in the object path to monitor and correct phase tilt resulting from angular misalignment between the sample and the optical axis. This mirror also ensures stable relative positioning across different samples by detecting deviations between the interference fringes produced by the mirror and those from the test object. Although physical alignment techniques substantially reduce system-induced errors, residual phase components such as tilt, curvature and high-order aberrations persist owing to mechanical limitations and the finite quality of optical components.

Here, we propose a hybrid compensation method to address phase aberrations arising from MO characteristics, system misalignment and component imperfections. A flat reference mirror serves as a target object to acquire a comprehensive phase-error map reflecting the cumulative aberrations of the entire system. The wavefront data obtained from the SH-WFS are decomposed into Zernike polynomials, accurately representing common aberration types, including tilt, defocus and higher-order distortions. The object's reconstructed phase map is then corrected by subtracting the total measured distortion, enabling accurate recovery of the true object phase. This integrated physical-digital approach simultaneously reduces both global and local system errors, yielding a reconstructed three-dimensional surface that more faithfully represents the true geometry of the measured object. Moreover, the SH-WFS data provide real-time feedback for system alignment optimisation, further minimising phase-error accumulation and enhancing overall measurement accuracy.

The theoretical foundation of the proposed phase-compensation procedure is outlined in Section 2. To validate its effectiveness, experiments were conducted using an MO with a 10 mm focal length. As detailed in Section 3, surface measurements on standard roughness samples with *Sa* values of 20.3 and 11.6 nm demonstrate the advantages of the proposed method.

## 2. Theoretical basis of the phase compensation technique

### *2.1. Phase aberration correction via 4f system alignment*

In the DHM system shown in Fig. 1, the MO is indispensable for image magnification. However, it also constitutes the primary source of spherical phase aberration.

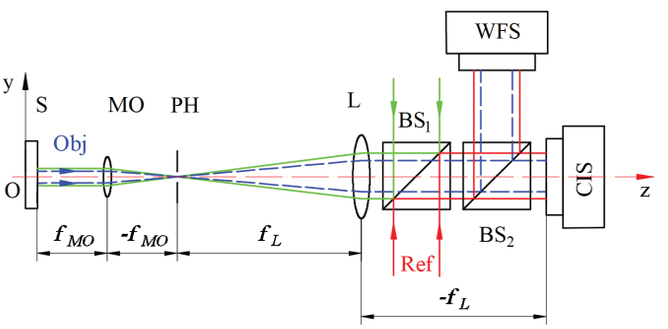


**Fig. 1. Principle of the infinity-corrected DHM system (4f configuration).** L: lens; BS: beam splitter; MO: microscope objective; PH: pinhole; S: specimen (object under measurement); M: flat mirror; Ref: reference wave; Obj: object wave. CIS: camera's image sensor; WFS: wavefront sensor. Source: The authors.

Under the paraxial approximation, the MO-induced spherical phase transformation can be mathematically expressed as follows [23]:

$$\varphi_{MO}(x,y) = (2-n)k\Delta + \frac{k(n-1)}{2}(x^2+y^2)\left(\frac{1}{R_1}-\frac{1}{R_2}\right) = (2-n)k\Delta + \frac{k}{2f}(x^2+y^2) \quad (1)$$

where λ represents the wavelength of the light source, and $k = 2\pi/\lambda$ is the wave number. $R_1$ and $R_2$ denote the radii of curvature of the MO's two spherical surfaces, while $n$, $\Delta$, and $f$ correspond to the refractive index, thickness, and focal length of the MO, respectively. From Eq. (1), as $f$ approaches infinity ($f=\infty$), in the afocal system formed by the compensating lens and the MO, the spherical phase term $\varphi_{MO} \approx (2-n)k\Delta$ becomes constant, indicating that the spherical phase distortion can be effectively eliminated.

To employ the MO for image magnification without altering the phase of the incident light, a straightforward optical arrangement known as the 4f system (Fig. 1) is used. In this configuration, the specimen (S) is positioned at the front focal plane of the MO. A compensating lens (L) is then arranged so that its front focal plane coincides with the rear focal plane of the MO, and the camera's imaging sensor (CIS) is located at the rear focal plane of L. The combined action of the MO and L thus behaves as a lens with an effective focal length of infinity, reducing aberrations introduced by the MO [4, 5, 14, 18]. Additionally, a pinhole is placed at the shared focal plane of L and the MO; it serves as a spatial-frequency low-pass filter, selectively blocking unwanted spatial frequencies according to its aperture size [24].

### *2.2. Phase aberration observation and removal using a wavefront sensor*

Accurate reconstruction of the object's three-dimensional surface profile using the 4f system shown in Fig. 1 requires that the object and reference waves be perfectly collimated, ensuring both beams remain parallel as they propagate through the optical system [4, 5, 14, 18]. To meet this requirement, the reference and object waves are maintained under identical environmental conditions, and the reference wave is collimated by adjusting the relative positions of the MO and lens L. Even under these conditions, residual aberrations may persist in the object wave owing to misalignment and imperfections in the optical components [16, 17, 19, 22].

To minimise phase aberrations in both waves, a calibration procedure is routinely carried out. The collimation quality of the reference wave is assessed using a Shack-Hartmann wavefront sensor (SH-WFS). The SH-WFS is placed at the position of mirror M in Fig. 1, with its surface plane perpendicular to the incident reference beam. The sensor's image array records the resulting spot pattern. The wavefront map which was analysed via Zernike-polynomial or spherical-fitting methods is used to determine the radius of curvature (RoC) and flatness deviation. The reference beam is considered well-collimated when the wavefront flatness and the Zernike coefficient $Z_4$ approach zero, and the RoC is very large. In this study, a RoC exceeding 22 metres is adopted as the criterion for acceptable collimation quality [25].

An analogous calibration is performed for the object wave. A precision flat mirror serves as the sample (S), and the SH-WFS captures the object-wavefront. By positioning the SH-WFS at the CIS location, the reference beam reflected from mirror M is blocked. The measured wavefront is then used to assess both the quality of the object wave and the surface structure of the flat mirror.

The cumulative phase aberration of the object wave comprises contributions from the reference-beam aberration, imperfections in the 4f system and optical aberrations of other system components. Consequently, adjustment of the relative positions of the object mirror, the MO and lens L allows optimisation to achieve the best possible wavefront flatness for the object wave.

## 3. Three-dimensional object profile reconstruction using digital off-axis holography and digital phase compensation

### *3.1. Phase map of object observation using digital off-axis holography and the Fourier transform method*

A right-handed Cartesian coordinate system *Oxyz* is defined, with the *Oz*-axis aligned along the optical axis connecting the centres of the two lenses (the MO and L), as shown in Fig. 1. The *Oxy*-plane corresponds to the imaging-sensor plane of the CIS camera, its origin *O* coinciding with the central pixel. The object plane is assumed to be parallel to the *Oxy*-plane. The hologram recorded at each pixel of the CIS is then described by the following equation [23]:

$$I(x,y) = |U_R|^2 + |U_O(x,y)|^2 + 2|U_R||U_O(x,y)|\cos[\varphi_{OH}(x,y) - \varphi_{OR}(x,y)] \quad (2)$$

where $\varphi_{OH}(x, y)$ and $\varphi_{OR}(x, y)$ represent the phases of the object wave and the reference wave, respectively, and

$$\varphi_H(x,y) = \varphi_{OH}(x,y) - \varphi_{OR}(x,y) = 2z(x,y)k + \varphi_C(x,y) + \varphi_A(x,y) \quad (3)$$

where $\varphi_H(x, y)$ is the phase extracted from the hologram, $z(x, y)$ is the object's depth, $\varphi_C(x, y)$ is the phase owing to the inclination of the reference mirror relative to the *Oxy*-plane, and $\varphi_A(x, y)$ is the aberration phase caused by imperfections in the object arm.

From the object hologram recorded by the CIS (Eq. (2)), the complex amplitude and phase of the object can be reconstructed following the procedure shown in Fig. 2, which involves four steps as implemented in [26]:

Step 1: Apply a Fourier transform to the recorded hologram, as depicted in Fig. 2A. The resulting spectrum includes the real image, the virtual image, and the zero-order term, as shown in Fig. 2B.

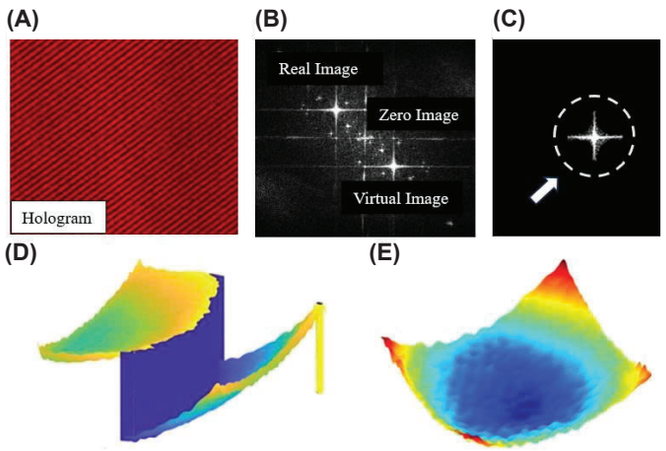


**Fig. 2. Fourier transform method for reconstructing the object profile from the recorded hologram. (A)** Recorded hologram of the object; **(B)** Frequency spectrum of the hologram; **(C)** Isolated object information using a spatial frequency band-pass filter; **(D)** Inverse Fourier transform producing the object's intensity image and wrapped phase; **(E)** Unwrapped phase of the object, which still contains the residual tilt phase component $\varphi_H(x, y)$. Source: The authors.

Step 2: Apply a spatial frequency band-pass filter to isolate the real image component from the full hologram spectrum. Then, shift this filtered component to the centre of the frequency domain, as shown in Fig. 2C. At this stage, the tilt of the reference phase $\varphi_R(x, y)$ is effectively removed [27].

Step 3: Perform an inverse Fourier transform on the centred real image (Fig. 2C) to obtain the object's intensity image and its corresponding phase map, as shown in Fig. 2D.

Step 4: The initial object phase obtained in Fig. 2D contains $2\pi$ discontinuities (wrapped phase). This wrapped phase is unwrapped to produce a continuous phase distribution, as shown in Fig. 2E.

Notably, the phase component $\varphi_C(x, y)$ in Eq. (3) is automatically removed from the object phase $\varphi_H(x, y)$ by shifting the real-intensity image of the object to the centre of the frequency domain [28]. Additionally, the aberration in the phase $\varphi_C(x, y)$ can be further eliminated from $\varphi_H(x, y)$ using the phase map obtained by the SH-WFS, as described in Section 2.2.

### *3.2. Reconstruction of the object's 3D profile with phase aberration compensation*

To accurately extract the depth information $z(x,y)$ from Eq. (3), the phase aberration $\varphi_A(x, y)$ must be minimised and removed from the measured phase $\varphi_H(x, y)$. As outlined in Sections 2.1 and 2.2, $\varphi_A(x, y)$ arises from imperfections in the collimated beam, misalignment between the MO and lens L, and optical aberrations in the system components shown in Fig. 1. Consequently, $\varphi_A(x, y)$ can be characterised using the SH-WFS with a precision flat mirror as the reference object. Once $\varphi_A(x, y)$ has been determined by the SH-WFS, (Section 2.1), the phase of the object mirror can be expressed using the following equation:

$$\varphi_{obj}(x, y) = \varphi_H(x, y) - \varphi_A(x, y) \quad (4)$$

and the depth information of the object follows from

$$z(x, y) = \varphi_{obj}(x, y)/(2k). \quad (5)$$

Because the reference object is a plane mirror, $\varphi_H(x, y)$ may be readily calculated and unwrapped following the procedure shown in Fig. 2. Based on the optical system shown in Fig. 1, the aberration phase $\varphi_A(x, y)$ must be determined using the object mirror and the SH-WFS. After replacing the mirror with the actual object, the reconstruction procedure described in Fig. 2 is repeated to obtain $\varphi_H(x, y)$, and Eq. (4) is used to subtract the aberration phase $\varphi_A(x, y)$.

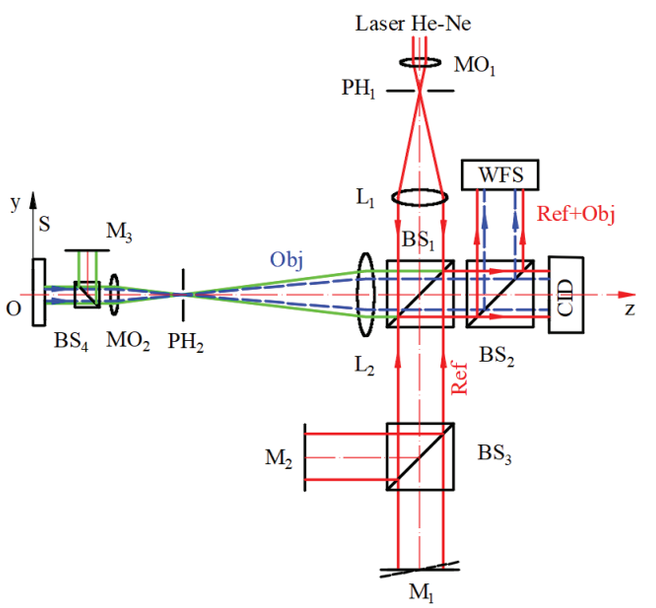


**Fig. 3. Schematic diagram of the experimental setup.** $L_1$: collimating lens; $L_2$: compensating lens; $BS_1$-$BS_4$: beam splitters; $MO_1$, $MO_2$: microscope objectives; $PH_1$, $PH_2$: pinholes; S: measured object; $M_1$-$M_3$: flat mirrors; CIS: camera's image sensor; WFS: wavefront sensor; Ref: reference wave; Obj: object wave. Source: The authors.

In practice, when the object mirror is replaced with the actual specimen, the SH-WFS is used both to assess the collimation of the reference wave and to measure the phase aberration $\varphi_A(x, y)$. However, owing to variations in measurement conditions, it can be challenging to obtain a highly accurate three-dimensional profile of the object. To address this, the optical arrangement of Fig. 1 is replaced by the hybrid setup shown in Fig. 3.

The system depicted in Fig. 3 employs a hybrid physical-digital phase-compensation strategy designed to minimise phase distortions introduced by optical components and to quantify residual phase errors after calibration. First, the laser source is focused through objective $MO_1$ onto pinhole $PH_1$. Lens $L_1$ then collimates the emerging beam into a plane wave. $PH_1$, positioned at the common focal plane of $MO_1$, has its diameter optimised to act as a spatial-frequency low-pass filter, thereby removing high-frequency noise from the laser emission [6]. The plane wave is split by beam splitter $BS_1$ into two paths: the reference beam (Ref) and the object-illumination beam.

The Ref beam is further split by the beam splitter $BS_3$. One portion transmits through $BS_3$, reflects off flat mirror $M_1$, then returns through $BS_3$ and $BS_1$ to reach $BS_2$. At $BS_2$, part of this beam proceeds directly to the CIS, while $BS_3$ reflects the remaining portion toward mirror $M_2$. Mirror $M_2$ reflects the beam back through the $BS_1$-$BS_2$ system, reaching both the CIS and the WFS.

The object-illumination beam is focussed through lens $L_2$ into the circular aperture $PH_2$ before entering $MO_2$ and beam splitter $BS_4$. $BS_4$ divides it into two paths: one directed to the object surface (S) and the other reflected towards mirror $M_3$, which serves as a reference surface for determining the compensating phase of the $MO_2$-$L_2$ optical path. The beam incident on S is collimated and, upon reflection, returns through the $MO_2$-$L_2$ system carrying the surface information. Since $PH_2$ acts as a low-pass spatial-frequency filter, the emergent beam from $L_2$ is a collimated wavefront bearing the object's phase information-referred to here as the object beam (Obj).

The Obj beam passes through beam splitter $BS_1$ and is then split at $BS_2$ into two paths: one directed to the WFS and the other to the CIS. At this stage, the CIS records the interference pattern between the Ref and Obj beams, thereby forming a hologram of the object surface S. Mirror $M_1$ introduces a controlled tilt angle $\theta$ between the Ref and Obj beams by adjusting its orientation. Mirror $M_2$, fixed and aligned parallel to the WFS and CIS planes, serves as a geometric reference during sample placement to eliminate the tilt phase $\varphi_C(x,y)$. Mirror $M_3$ is likewise aligned parallel to $M_2$. When the object is replaced, surface S is carefully aligned parallel to $M_2$ by monitoring the interference fringes formed between them. This ensures consistent and stable positioning across different measurement samples.

Figure. 3 illustrates the incorporation of plane mirrors $M_2$ and $M_3$ into the optical system to minimise and characterise the phase aberration $\varphi_A(x, y)$. By blocking the light reflected from both the object arm and mirror $M_2$, the collimation quality of the reference wave from mirror $M_1$ may be assessed using the SH-WFS. Conversely, by blocking the reference arm and the light reflected from object S, mirror $M_2$ becomes the target, enabling the SH-WFS to measure $\varphi_A(x, y)$. When the light from mirrors $M_2$ and $M_3$ is blocked, the CIS records the hologram formed by interference between object S and the reference mirror $M_1$. The phase $\varphi_H(x, y)$ is then extracted from this hologram using the procedure described in Fig. 2. By applying Eqs. (4) and (5), the 3D profile of the object can be accurately reconstructed. Importantly, both mirror $M_3$ and object S in Fig. 3 are positioned at the focal plane of the objective lens $MO_2$.

## 4. Experiments and results

### *4.1. Experimental setup*

To evaluate the performance of the proposed method, the optical system of Fig. 3 was realised in the configuration shown in Fig. 4. Experiments were performed on an LTB4-1208 vibration-isolated optical table. A modular mounting system combined with a precision three-axis translation stage ensured accurate alignment of all optical components.

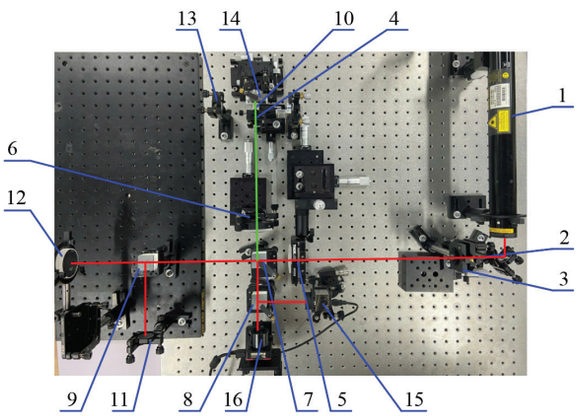


**Fig. 4. Experimental setup layout.** 1: He-Ne laser; 2: Microscope objective $MO_1$ (60×); 3: Pinhole $PH_1$ (10 µm); 4: AL1210M lens ($f$=10 mm) and pinhole $PH_2$ (2 mm); 5: Collimating lens $L_1$ ($f$=300 mm); 6: Compensating lens $L_2$ ($f$=200 mm); 7-10: Beam splitters $BS_1$-$BS_3$; 11-13: Plane mirrors; 14: Sample; 15: Wavefront sensor; 16: Camera. Source: The authors.

The light source was a He-Ne laser (05-LHP-991, Melles Griot) with a wavelength of λ=632.8 nm. Pinhole $PH_1$ (P10K, Thorlabs), positioned at the focal plane of $MO_1$ (5721-A-H, Newport), had a diameter of 10 µm, and the collimating lens $L_1$ (ACT508-300-A, Thorlabs) had a focal length of $f_{L1}$=300 mm. The image sensor used was a CS165MU1 (Thorlabs) camera with a resolution of 1,440×1,080 pixels and a pixel size of 3.45×3.45 µm. The compensating lens $L_2$ (ACT508-200-A, Thorlabs) had a focal length of $f_{L2}$=200 mm. The aspheric lens AL1210M-A (Thorlabs), serving as $MO_2$, had a focal length of $f_{MO2}$=10 mm and a numerical aperture (NA) of 0.55.

The inclination angle θ between the object and reference waves was adjusted in the range of $0.48° \leq \theta \leq 5.3°$ [23]. This setup produced a system magnification of 20×, satisfying the criteria for diffraction-limited performance [27].

### *4.2. Experimental calibration and phase error measurement of the system*

From the optical setup in Fig. 4, the system's phase error was first reduced by specifying the beam profile of the reference wave. To achieve this, the light from the object arm and the reference mirror $M_1$ was blocked, allowing the collimated beam reflected from mirror $M_2$ to be observed by the SH-WFS for reconstructing the reference beam profile. The flatness of the beam was then evaluated using the root mean square (RMS) and peak-to-valley (PV) values based on the measured reference beam profile. A well-collimated reference beam is indicated by minimal RMS and PV. By adjusting the positions of $PH_1$ and $L_1$, the optimal collimated profile of the reference beam was achieved (Fig. 5A).

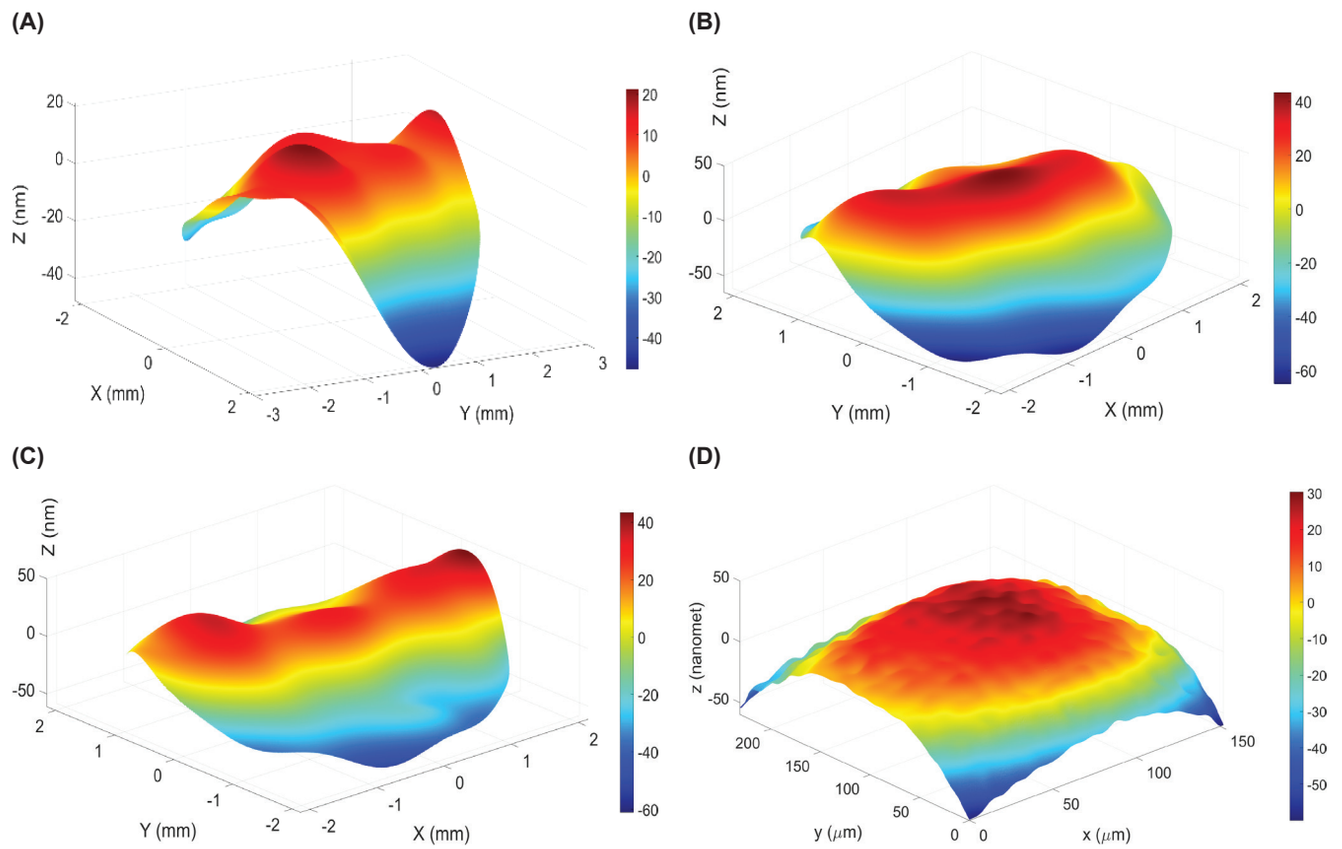


**Fig. 5. Reference wavefront and object wavefront measured by the wavefront sensor (WFS) after system alignment. (A)** Reference wavefront reflected from mirror $M_2$, with peak-to-valley (PV)=0.105 λ and root mean square (RMS)=0.092 λ; **(B)** Object wavefront reflected from mirror $M_3$, with PV=0.177 λ and RMS=0.083 λ; **(C)** Total system phase error $\varphi_A(x,y)$ determined by subtracting **(A)** from **(B)**, PV=0.165 λ and a root mean square (RMS)=0.043 λ; **(D)** The object wavefront retrieved from mirror M3 using the Fourier transform method yielded PV=0.177 λ and a root mean square (RMS)=0.083 λ. Source: The authors.

Subsequently, the reference arm and the light reflected from the sample S were blocked, and the profile of the object mirror $M_3$ was recorded with the SH-WFS. The positions of $MO_2$ and $M_3$ were tuned to minimise the RMS and PV of the $M_3$ profile, thereby optimising the alignment of $M_3$, $MO_2$, $L_2$, and the SH-WFS for the 4f system. The resultant $M_3$ profile, derived from the object-wave wavefront, is shown in Fig. 5B. Because the flat mirror $M_3$ is assumed to be perfectly flat, the difference between the profiles in Figs. 5A and 5B, shown in Fig. 5C, corresponds directly to $\varphi_A(x, y)$, representing the phase aberration of the optical system.

By blocking the light from mirror $M_2$, the hologram, formed by the interference pattern between the object wave reflected from $M_3$ and the reference wave reflected from $M_1$-was recorded. The object profile of $M_3$ was reconstructed from this hologram using the Fourier transform method depicted in Fig. 2 and is shown in Fig. 5D. In this reconstruction, the profile was obtained using Eq. (5), where $\varphi_H(x, y)$ was calculated from the hologram. Because the object is a mirror, the relationship $\varphi_A(x, y)=-\varphi_H(x, y)$ holds.

Although the profiles in Fig. 5C and 5D should coincide for an ideally flat mirror, the observed discrepancy is acceptable. This difference arises chiefly because fitting the wavefront with *Zernike* polynomials filters out small random noise and complex surface features introduced by environmental fluctuations or optical imperfections. Moreover, the lateral resolution achieved through hologram reconstruction is considerably higher than that obtained by the SH-WFS [29]. Given the inherent limitations of Zernike-based methods [6], the profile reconstructed from the hologram was adopted to compensate for the optical system's phase aberration.

### *4.3. Surface profile measurement experiment*

In this experiment, the profiles of two test objects were measured to assess the performance of the proposed optical system. Prior to observation with this system, their profiles were verified using a Zygo ZeGage™ Pro 3D surface profiler, which provides an axial resolution of 0.15 nm and a lateral resolution of 0.52 µm. Measurement results (Figs. 6A and 6B) yielded roughness values of *Sa*=17.95 and *Sa*=11.58 nm, respectively.

Subsequently, holograms of the two objects were recorded with the CMOS camera and reconstructed via the Fourier-transform method. The reconstructed profiles (Figs. 7A and 7C) produced surface roughness values of *Sa*=16.2 and *Sa*=10.42 nm, respectively, using standard procedures [30].

Using the object-mirror profile from Fig. 5D, the profiles in Figs. 7A and 7C were compensated. The resulting compensated profiles (Figs. 7B and 7D) show the corrected surface geometries and their respective roughness values. To ensure statistical reliability, each object was measured 50 times; the averaged results are summarised in Table 1.

**Table 1. Object roughness measured by ZeGage™ Pro and the proposed method.**

| Sample no. | Measurement result by ZeGage™ Pro (nm) | Experimental result (nm) |
|---|---|---|
| 1 | 17.95±0.52 | 16.2±0.85 |
| 2 | 11.58±0.16 | 10.42±0.61 |

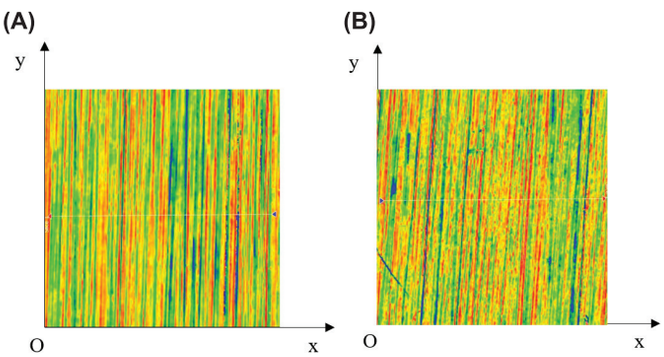


**Fig. 6. Measurement results of the roughness samples using the ZeGage™ Pro system (Zygo). (A)** Roughness sample with measured *Sa*=17.95 nm; **(B)** Roughness sample with measured *Sa*=11.58 nm. Source: The authors.

## 5. Conclusions

In this study, we have demonstrated both theoretically and experimentally the effectiveness of the proposed phase-compensation technique in a DHM system. This approach combines physical and digital methods with wavefront measurements using an SH-WFS and was evaluated using various sample types.

The physical compensation strategy minimised phase aberration in a telecentric configuration by aligning the system with the aid of the SH-WFS and fixing a reference mirror ($M_2$) in the object path to ensure consistent angular alignment across samples. The digital method complemented this by quantifying the residual phase error using a flat reference mirror ($M_3$) placed in the object arm.

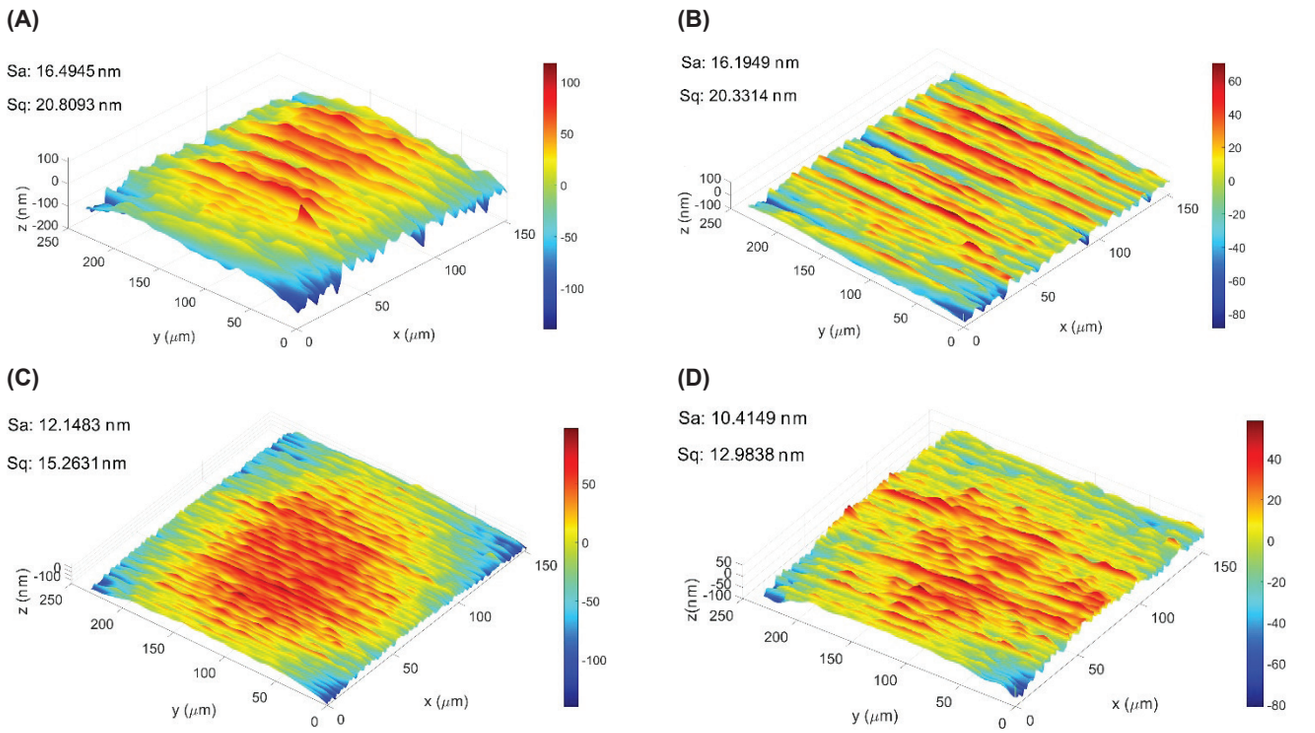


**Fig. 7**. **Measurement results of the actual objects. (A, B)** 3D surface reconstruction of the sample with *Sa*=16.2 nm, before and after digital phase compensation, respectively. **(C, D)** 3D surface reconstruction of the sample with *Sa*=10.42 nm, before and after digital phase compensation, respectively. Source: The authors.

Our results showed that the residual phase error was small and remained stable over time and across repeated measurements. To achieve these outcomes, we employed a comprehensive framework encompassing phase unwrapping, noise suppression, measurement-error correction and three-dimensional surface visualisation. This framework enabled high-precision surface profiling, detecting height variations at the nanometre scale with excellent accuracy. The results demonstrate the advantages of holographic techniques in general and the robustness of the proposed method in particular.

Nevertheless, challenges persisted when measuring surfaces with $Sa \leq 2$ nm owing to limitations in optical-component quality and the current inability to eliminate all noise from the optical system and the measured surface. Once these issues are addressed, the proposed DHM system holds strong potential for the accurate characterisation of finely polished optical surfaces.

## CRediT author statement

Pham Duc Tuan: Conceptualisation, Experiment, Writing original draft, Data processing; Vu Thanh Tung: Methodology, Formal analysis, Investigation, Supervision; Phan Dinh Tuan: Experiment, Experimental data processing; Bui Thanh Tung, Mai Linh: Writing - Reviewing and Editing, Validation; Pham Ngoc Thao: Writing - Reviewing and Editing, Validation; Duong Minh Ngoc: Experimental data processing; Pham Duc Quang: Methodology, Writing - Reviewing and Editing, Validation, Formal analysis, investigation, Supervision.

## ACKNOWLEDGEMENTS

This research is funded by the Vietnam National Foundation for Science and Technology Development (NAFOSTED) under grant number 14/2022/TN.

## COMPETING INTERESTS

The authors declare that there is no conflict of interest regarding the publication of this article.

## REFERENCES

[1] V. Petrov, A. Pogoda, V. Sementin, et al. (2022) "Review advances in digital holographic interferometry", *Imaging*, **8**, DOI: 10.3390/jimaging8070196.

[2] A.G. Marrugo, F. Gao, S. Zhang (2020), "State-of-the-art active optical techniques for three-dimensional surface metrology: A review", *Journal of The Optical Society of America A*, **37**, pp.60-77, DOI: 10.1364/JOSAA.398644.

[3] R. Castañeda, C. Trujillo, A. Doblas (2020), "pyDHM: A Python library for applications in digital holographic microscopy", *PLOS ONE*, **17(10)**, DOI: 10.1371/journal.pone.0275818.

[4] R. Castañeda, J.G. Sucerquia (2022), "Single-shot 3D topography of transmissive and reflective samples with a dual-mode telecentric-based digital holographic microscope", *Sensors*, **22**, DOI: 10.3390/s22103793.

[5] D.N. Deng, J.Z. Peng, W.J. Qu, et al. (2017), "Simple and flexible phase compensation for digital holographic microscopy with electrically tunable lens", *Applied Optics*, **56**, pp.6007-6014, DOI: 10.1364/AO.56.006007.

[6] L. Huang, L. Yan, B. Chen, et al. (2020), "Phase aberration compensation of digital holographic microscopy with curve fitting preprocessing and automatic background segmentation for microstructure testing", *Optics Communications*, **462**, DOI: 10.1016/j.optcom.2020.125311.

[7] W. Osten, P. Ferraro (2019), *Optical Inspection of Microsystems*, CRC Press, DOI: 10.1201/9781420019162.

[8] A. Asundi (2011), *Digital Holography for MEMS and Microsystem Metrology*, Wiley, DOI: 10.1002/9781119997290.

[9] T. Namazu (2023), "Mechanical property measurement of micro/nanoscale materials for MEMS: A review", *IEEJ Transactions on Electrical and Electronic Engineering*, **18(3)**, pp.308-324, DOI: 10.1002/tee.23747.

[10] M.V. Fernandez, E. Goncalves, J.L.V. Rivera, et al. (2018), "Development of digital holographic microscopy by reflection for analysis of surface", *Results Phys*., **11**, pp.182-187, DOI: 10.1016/j.rinp.2018.08.050.

[11] Y. Emery, T. Colomb, E. Cuche (2021), "Metrology applications using off-axis digital holographic microscopy", *Journal of Physics: Photonics*, **3(3)**, DOI: 10.1088/2515-7647/ac0957.

[12] M.M.E. Beheiry, J.R. McGorty, B. Huang (2024), "Imaging of live cells by digital holographic microscopy", *Photonics*, **5(1)**, pp.1-18, DOI: 10.3390/photonics11100980.

[13] K.L.V. Werth, B. Kemper, S. Kampmeier, et al. (2023), "Application of digital holographic microscopy to analyze changes in T-cell morphology in response to bacterial challenge", *Cells*, **12(5)**, DOI: 10.3390/cells12050762.

[14] T. Nguyen, G. Nehmetallah, C. Raub, et al. (2016), "Accurate quantitative phase digital holographic microscopy with single and multiple-wavelength telecentric and nontelecentric configurations", *Appl. Opt.*, **55**, pp.5666-5683, DOI: 10.1364/ao.55.005666.

[15] Z. Ren, J. Zhao, E.Y. Lam (2019), "Automatic compensation of phase aberrations in digital holographic microscopy based on sparse optimization", *APL Photonics*, **4(11)**, DOI: 10.1063/1.5115079.

[16] D.G. Sirico, L. Miccio, Z. Wang, et al. (2022), "Compensation of aberrations in holographic microscopes: Main strategies and applications", *Applied Physics B*, **128(78)**, DOI: 10.1007/s00340-022-07798-8.

[17] W. Lyu, Y. Shi (2024), "Efficient phase aberration compensation for digital holographic microscopy based on aberration-oriented phase unwrapping", *Optics Communications*, **554**, DOI: 10.1016/j.optcom.2023.130212.

[18] A. Doblas, E.S. Ortiga, M.M. Corral, et al. (2014), "Accurate single-shot quantitative phase imaging of biological specimens with telecentric digital holographic microscopy", *J. Biomed. Opt.*, **19**, DOI: 10.1117/1.jbo.19.4.046022.

[19] D. Deng, W. Qu, W. He, et al. (2017), "Off-axis tilt compensation in common-path digital holographic microscopy based on hologram rotation", *Optics Letters*, **42(24)**, pp.5282-5285, DOI: 10.1364/OL.42.005282.

[20] T. O'Connor, J.B. Shen, B.T. Liang, et al. (2021), "Digital holographic deep learning of red blood cells for field-portable, rapid COVID-19 screening", *Opt. Lett.*, **46**, pp.2344-2347, DOI: 10.1364/OL.426152.

[21] J.B. Shohani, M. Hajimahmoodzadeh, H. Fallah (2023), "Using a deep learning algorithm in image-based wavefront sensing: Determining the optimum number of Zernike terms", *Optics Contin.*, **2**, pp.632-645, DOI: 10.1364/OPTCON.485330.

[22] H. Jeon, M. Jung, G. Lee, et al. (2023), "Aberration estimation for synthetic aperture digital holographic microscope using deep neural network", *Sensors*, **23**, DOI: 10.3390/s23229278.

[23] J.W. Goodman (2005), *Introduction to Fourier Optics*, Roberts and Company Publishers, 116pp.

[24] Y. Deng, C.H. Huang, B. Vinoth, et al. (2020), "A compact synthetic aperture digital holographic microscope with mechanical movement-free beam scanning and optimized active aberration compensation for isotropic resolution enhancement", *Optics and Lasers in Engineering*, **134**, DOI: 10.1016/j.optlaseng.2020.106251.

[25] M. Chen, F.S. Roux, J.C. Olivier (2007), "Detection of phase singularities with a Shack-Hartmann wavefront sensor", *J. Opt. Soc. Am. A*, **24**, pp.1994-2002, DOI: 10.1364/JOSAA.24.001994.

[26] P.D. Tuan, V.T. Tung, H.A. Tu, et al. (2024), "3D measurement of surface profile using holography technique and Fourier transform method", *Journal of Military Science and Technology*, **98**, pp.132-138, DOI: 10.54939/1859-1043.j.mst.98.2024.132-138 (in Vietnamese).

[27] U. Schnars, W.P.O. Jüptner (2002), "Digital recording and numerical reconstruction of holograms", *Meas. Sci. Technol*., **13**, pp.R85-R101, DOI: 10.1088/0957-0233/13/9/201.

[28] U. Schnars, W. Jüptner (2002), *Digital Holography: Digital Hologram Recording, Numerical Reconstruction, and Related Techniques*, Springer, 174pp.

[29] E.S. Ortiga, A. Doblas, G. Saavedra, et al. (2014), "Off-axis digital holographic microscopy: Practical design parameters for operating at diffraction limit", *Appl. Opt.*, **53**, pp.2058-2066, DOI: 10.1364/AO.53.002058.

[30] International Organisation for Standardisation (2012), *Geometrical Product Specifications (GPS) - Surface Texture: Areal - Part 2: Terms, Definitions and Surface Texture Parameters* (ISO 25178-2).